

## Laboratory and astronomical discovery of magnesium dicarbide, MgC<sub>2</sub>

P. B. CHANGALA,<sup>1</sup> H. GUPTA,<sup>1,2</sup> J. CERNICHARO,<sup>3</sup> J. R. PARDO,<sup>3</sup> M. AGÚNDEZ,<sup>3</sup> C. CABEZAS,<sup>3</sup> B. TERCERO,<sup>4</sup>  
M. GUÉLIN,<sup>5</sup> AND M. C. MCCARTHY<sup>1</sup>

<sup>1</sup>*Center for Astrophysics | Harvard & Smithsonian, Cambridge, MA 02138, USA*

<sup>2</sup>*National Science Foundation, Alexandria, VA 22314, USA*

<sup>3</sup>*Instituto de Física Fundamental, CSIC, Department of Molecular Astrophysics, Serrano 121, 28006 Madrid, Spain*

<sup>4</sup>*Observatorio Astronómico Nacional, IGN, C/Alfonso XII 3, 28014 Madrid, Spain*

<sup>5</sup>*Institut de Radioastronomie Millimétrique, 300 rue de la Piscine, 38406 Saint Martin d'Hères, France*

### ABSTRACT

We report the detection of magnesium dicarbide, MgC<sub>2</sub>, in the laboratory at centimeter wavelengths and assign <sup>24</sup>MgC<sub>2</sub>, <sup>25</sup>MgC<sub>2</sub>, and <sup>26</sup>MgC<sub>2</sub> to 14 unidentified lines in the radio spectrum of the circumstellar envelope of the evolved carbon star IRC+10216. The structure of MgC<sub>2</sub> is found to be T-shaped with a highly ionic bond between the metal atom and the C<sub>2</sub> unit, analogous to other dicarbides containing electropositive elements. A two-temperature excitation model of the MgC<sub>2</sub> emission lines observed in IRC+10216 yields a very low rotational temperature of  $6 \pm 1$  K, a kinetic temperature of  $22 \pm 13$  K, and a column density of  $(1.0 \pm 0.3) \times 10^{12}$  cm<sup>-2</sup>. The abundance of MgC<sub>2</sub> relative to the magnesium-carbon chains MgCCH, MgC<sub>4</sub>H, and MgC<sub>6</sub>H is 1:2:22:20 and provides a new constraint on the sequential radiative association-dissociative recombination mechanisms implicated in the production of metal-bearing molecules in circumstellar environments.

### 1. INTRODUCTION

Silicon dicarbide (SiC<sub>2</sub>) was long known to exist in carbon-rich stellar atmospheres (Kleman 1956, and references therein), but its identification as the carrier of nine unassigned lines in the radio spectrum of the archetype carbon star IRC+10216 was a key advance in understanding the molecular constituents of evolved carbon stars (Thaddeus et al. 1984). Its substantial abundance and the highly ionic nature of the Si–C<sub>2</sub> bond suggested that molecules containing other electropositive elements bonded to C<sub>2</sub> or longer carbon chains might be present in IRC+10216 and responsible for other unidentified lines there. In the nearly 40 years since the radio astronomical identification of SiC<sub>2</sub>, a number of metal-bearing molecules have been discovered in IRC+10216, most containing strong ionic bonds between metal atoms and carbon chains (Cernicharo et al. 2019; Pardo et al. 2021). It is surprising, therefore, that metal dicarbides — the simplest molecules containing one metal atom and two carbon atoms — are absent from this inventory. Although several metal dicarbides have now been studied in the laboratory, accurate data are available only for one (AlC<sub>2</sub>) (Halfen & Ziurys 2018, & references therein) that is a plausible candidate for radio astronomical detection.

Magnesium dicarbide (MgC<sub>2</sub>) is an excellent candidate for detection in IRC+10216 because of the high

cosmic abundance of magnesium, which is found in nearly half of all known metal-bearing species in this source. An early theoretical study of MgC<sub>2</sub> (Green 1984) predicted a triangular, symmetric, and highly polar ground-state structure similar to SiC<sub>2</sub>. Motivated by the discoveries of MgNC and MgCN several years later (Kawaguchi et al. 1993; Ziurys et al. 1995), more accurate calculations of MgC<sub>2</sub> appeared in the literature (Itono et al. 2000), but no gas-phase measurements followed. The purpose of this Letter is to report the laboratory detection of MgC<sub>2</sub> at centimeter wavelengths, and its assignment to a series of previously unidentified lines in the radio spectrum of IRC+10216. To our knowledge, this is the first spectroscopic characterization of MgC<sub>2</sub> in any wavelength region, while its astronomical discovery fills a longstanding gap in the molecular inventory of evolved carbon stars.

### 2. LABORATORY MEASUREMENTS

Rotational lines of MgC<sub>2</sub> were detected with a Fourier transform microwave (FTMW) spectrometer coupled to a laser ablation supersonic expansion source previously used in our laboratory to characterize small metal-containing molecules (Brünken et al. 2008; Zingsheim et al. 2017; Lee et al. 2019). A rotating magnesium rod was ablated by 50-mJ pulses of 532-nm radiation from an Nd:YAG laser operating at 5 Hz. The ablated

Mg atoms were entrained in a dilute mixture (0.1%) of acetylene in neon, which then passed through two copper discharge electrodes. An 800-V discharge struck between the electrodes increased the product yield by up to a factor of 5 (Sun et al. 2010). After expanding into a large vacuum chamber, the molecules were polarized in a co-axially aligned cavity spectrometer operating from 5 to 26 GHz (Grabow et al. 2005; Crabtree et al. 2016). Double-resonance transitions at higher frequencies were driven by microwave horns placed perpendicular to the cavity axis.

The identification of  $\text{MgC}_2$  was challenging because only one transition, the  $1_{01} - 0_{00}$  line predicted to lie near 20.9 GHz (Itono et al. 2000), falls within our spectrometer bandwidth. After optimizing the production of  $\text{MgCCH}$ , we conducted a search from 20.4 to 21.0 GHz. This survey was extremely sparse, with only a single ablation-dependent feature at 20896 MHz, shown in Fig. 2, close to the prediction of 20892 MHz from quantum chemical calculations performed for this work (see Appendix A). We conducted a number of assays to test the carrier of this line: the signal was unaffected by applied magnetic fields, consistent with the predicted closed-shell ground electronic state; it required the presence of acetylene, but was unaffected by replacing  $\text{HCCH}$  with  $\text{DCCD}$ , indicating it contains carbon but not hydrogen; and the relative intensity from a statistical  $^{12}\text{C}/^{13}\text{C}$   $\text{HCCH}$  precursor suggested it likely contained only two C atoms. Spectroscopic confirmation was provided by the observation of a double resonance transition ( $2_{02} - 1_{01}$ , top panel of Fig 2) at its expected frequency near 41.7 GHz. Assuming a dipole moment of 7.9 D (Itono et al. 2000), we estimate the number of  $\text{MgC}_2$  molecules in each gas pulse to be  $4 \times 10^8$ , significantly less abundant than  $\text{MgCCH}$  ( $5 \times 10^{10}$ ) or the precursor Mg atoms ( $5 \times 10^{14}$ , estimated from the ablation target mass loss) and  $\text{HCCH}$  ( $2 \times 10^{15}$ , from calibrated flow meters).

With the assignment of  $\text{MgC}_2$  secure, we proceeded to search for its isotopologues. The fundamental transitions of  $^{26}\text{Mg}^{12}\text{C}_2$  and  $^{25}\text{Mg}^{12}\text{C}_2$  were detected in natural abundance, while those of  $^{24}\text{Mg}^{13}\text{C}^{12}\text{C}$  and  $^{24}\text{Mg}^{13}\text{C}_2$  were detected using a  $^{13}\text{C}$ -enriched sample of acetylene. Their transition frequencies are shown in Table 1 and are uniformly within 0.5 MHz of the theoretical isotopic shifts. These laboratory measurements are insufficient to determine the  $A$ ,  $B$ , and  $C$  rotational constants for each isotopologue independently, but together provide enough information to derive a semi-experimental equilibrium structure, shown in Fig. 1 (see Appendix A for details). The  $1_{01} - 0_{00}$  transition of  $^{25}\text{Mg}^{12}\text{C}_2$  is split into three hyperfine compo-

nents by nuclear electric quadrupole interactions. The observed coupling constants are  $\chi_{aa} = -11.75(2)$  MHz and  $\chi_{bb} = 4.8(10)$  MHz, which agree well with the theoretical predictions of  $-11.4$  MHz and  $4.8$  MHz, respectively.

### 3. ASTRONOMICAL IDENTIFICATION

With accurate laboratory data in hand, we examined available spectroscopic surveys and observations of IRC+10216 for evidence of  $\text{MgC}_2$ . An unidentified rotational line, U41712, coincident with the  $2_{02} - 1_{01}$  transition of  $^{24}\text{MgC}_2$  was found in the recent 6–10 millimeter survey done by Pardo et al. (2022) using the Yebes 40 m telescope. A second unidentified line, U82788, was found in a study reporting the identification of the  $\text{HC}_4\text{N}$  radical (Cernicharo et al. 2004) using the IRAM 30 m telescope. Subsequently, 8 additional unidentified lines were quickly found in unpublished surveys at 2 and 3 millimeters done with the IRAM 30 m telescope (see Cernicharo et al. (2019) for details) and assigned to  $^{24}\text{MgC}_2$ . One line of  $^{25}\text{MgC}_2$  and three lines of  $^{26}\text{MgC}_2$  were also found at precisely the expected isotopic shifts.

There is overwhelming evidence that  $\text{MgC}_2$  is the carrier of the lines listed in Table 2 and displayed in Figures 3 and 4. As Table 2 shows, a combined fit of the observed laboratory and astronomical lines of  $^{24}\text{MgC}_2$  to Watson’s  $A$ -reduced Hamiltonian yields small residuals corresponding to a normalized rms of 1.37 (Table 3), demonstrating that they originate from the same molecule. Table 3 lists the spectroscopic constants derived using only six free parameters (three rotational constants and three centrifugal distortion constants) and two parameters fixed to theoretical values. Similarly small residuals are obtained for  $^{25}\text{MgC}_2$  and  $^{26}\text{MgC}_2$ , albeit with fewer determinable parameters given the small data sets. The ratio of the integrated intensities of the  $2_{02} - 1_{01}$  lines of the three isotopologues is  $(73 \pm 5):(11 \pm 2):(15 \pm 3)$ , consistent with the solar abundance ratio of  $^{24}\text{Mg}:^{25}\text{Mg}:^{26}\text{Mg}$  of  $(79.2 \pm 0.6):(9.5 \pm 0.5):(11.3 \pm 0.5)$  (Bochsler et al. 1996) and the abundance ratio derived for  $\text{MgNC}$  in IRC+10216 itself,  $(78 \pm 2):(11 \pm 1):(11 \pm 1)$  (Guélin et al. 1995).

Figures 3 and 4 present the astronomical spectra and show that the assigned lines meet all requirements of the identification. Each line exhibits the same double-peaked or “U-shaped” profile and has the same width as the strong  $4_{04} - 3_{03}$  line ( $29.0 \pm 0.5 \text{ km s}^{-1}$ ) to within observational uncertainties. Six fully resolved or nearly fully resolved lines and four partially blended lines of  $^{24}\text{MgC}_2$  are detected. Three lines of  $^{26}\text{MgC}_2$  are detected, including one which is partially blended. Finally, one line of  $^{25}\text{MgC}_2$  is detected with a slightly broadened

line width consistent with the underlying quadrupole hyperfine structure predicted from the laboratory measurements. The high quality profiles derived from the resolved lines and the precise rest frequencies of the blended lines allow us to account for the contributions of the interlopers and extract reliable parameters.

We have analyzed the intensities of the rotational lines to infer the excitation of the molecules on two assumptions: (1) to correct for the changing antenna beamwidth in Table 2, it is assumed by analogy with other Mg-bearing molecules in IRC+10216, that the  $\text{MgC}_2$  emission is confined to a shell of  $30''$  in diameter (Cernicharo et al. 2019; Pardo et al. 2021), an assumption supported by the U-shaped profiles of the lines and (2) all of the lines in Table 2 are optically thin because of their faintness.

#### 4. DISCUSSION

As Figure 1 shows, rotational emission lines spanning a wide range in energy are detected in IRC+10216, allowing us to construct the rotational temperature diagram shown in Fig. 5. The integrated intensities of the lines are reproduced by a simple two-temperature excitation model (see Appendix B) in which a temperature  $T_{\text{rot}} = 6 \pm 1$  K describes the relative populations within each  $K$  ladder and  $T_{\text{kin}} = 22 \pm 13$  K describes the relative populations across  $K$  ladders and provides a measure of the gas kinetic temperature. A comparison of the derived excitation temperatures of  $\text{MgC}_2$ ,  $\text{SiC}_2$ , and  $\text{SiC}_3$  shows that  $T_{\text{rot}}$  is similar for the three species ( $6 \pm 1$  K vs. 10 K and 13 K (Thaddeus et al. 1984; Apponi et al. 1999)), but  $T_{\text{kin}}$  is not. The latter is similar for  $\text{MgC}_2$  and  $\text{SiC}_3$  ( $22 \pm 13$  K and 46 K (Apponi et al. 1999)), and it is significantly smaller than for  $\text{SiC}_2$  (140 K (Thaddeus et al. 1984)), probably because  $\text{MgC}_2$  and  $\text{SiC}_3$  reside in the cool outer envelope of IRC+10216, whereas  $\text{SiC}_2$  is more widely distributed, residing in the warmer inner regions as well as the outer envelope (Patel et al. 2011). The  $T_{\text{kin}}$  of 22 K inferred for  $\text{MgC}_2$  is remarkably close to the value of 20 K inferred from observations and modeling of dust, CO, and CCH in the  $30''$ – $40''$  diameter shell of IRC+10216 (Guélin et al. 2018). As discussed in Appendix B, the column density averaged over a  $30''$  antenna beam is  $N(\text{MgC}_2) = 1 \times 10^{12} \text{ cm}^{-2}$ , with an estimated uncertainty of 30%, corresponding to a fractional abundance of  $\sim 5 \times 10^{-10}$  relative to  $\text{H}_2$ .<sup>1</sup>

On the assumption that  $\text{MgC}_2$  is co-spatial with the magnesium-carbon chain radicals  $\text{MgCCH}$ ,  $\text{MgC}_4\text{H}$  and  $\text{MgC}_6\text{H}$  (which is supported by the similar line profiles),

a comparison of their abundances might shed light on the production of Mg-bearing species in the outer envelope of IRC+10216. The formation of  $\text{MgCCH}$ ,  $\text{MgC}_4\text{H}$  and  $\text{MgC}_6\text{H}$  has been explained by a two-step process in which radiative association (RA) of  $\text{Mg}^+$  with large polyynes  $\text{HC}_{2n}\text{H}$  ( $n \geq 4$ ) yields the intermediate ions  $\text{MgHC}_{2n}\text{H}^+$ , which then undergo dissociative recombination (DR) to yield the neutral radicals (Cernicharo et al. 2019; Pardo et al. 2021). This mechanism, originally proposed by Petrie (1996) and later expanded by Dunbar & Petrie (2002), is thought to control the formation of the metal cyanides and acetylides detected in IRC+10216 (Millar 2008; Cabezas et al. 2013; Cernicharo et al. 2019; Pardo et al. 2021). The chemical models developed in these studies indicate that the main precursors of magnesium carbon chains are large  $\text{MgHC}_{2n}\text{H}^+$  complexes with more than six carbon atoms. If, as is plausible,  $\text{MgC}_2$  is also a fragmentation product in the DR of  $\text{MgHC}_{2n}\text{H}^+$ , then the observed column density ratio  $\text{MgC}_2:\text{MgCCH}:\text{MgC}_4\text{H}:\text{MgC}_6\text{H} = 1:2:22:20$  provides a useful constraint on the relative yields of the DR of the parent ions. Observations of other plausible DR products, such as  $\text{MgC}$  and larger  $\text{MgC}_n$  clusters are needed to better elucidate the poorly constrained gas-phase chemistry. A parallel formation mechanism that may also be important is the RA-DR of  $\text{Mg}^+$  and large cyanopolynes,  $\text{HC}_{2n+1}\text{N}$  (Dunbar & Petrie 2002). Experimental measurements of the branching ratios of the various fragments formed in the DR of large  $\text{MgHC}_{2n}\text{H}^+$  and  $\text{MgHC}_{2n+1}\text{NH}^+$  ions would enable a direct comparison against the observed abundance ratios, permitting a holistic assessment of the production of metal-bearing molecules in the outer layers of IRC+10216.

Understanding the structure and bonding in metal dicarbides is of fundamental chemical interest and may identify additional metal carbides that are candidates for astronomical detection. Like other T-shaped triatomic dicarbides, including  $\text{SiC}_2$  (Cernicharo et al. 1991),  $\text{GeC}_2$  (Zingsheim et al. 2017),  $\text{BeC}_2$  (Green et al. 2020),  $\text{AlC}_2$  (Halfen & Ziurys 2018),  $\text{ScC}_2$  (Min et al. 2014), and  $\text{YC}_2$  (Halfen et al. 2013),  $\text{MgC}_2$  exhibits an ionic metal-carbon bond best described as  $\text{Mg}^+-\text{C}_2^-$ . Its equilibrium CC bond length,  $r_{\text{CC}} = 1.2706(7) \text{ \AA}$ , is close to that of bare  $\text{C}_2^-$  itself,  $r_{\text{CC}} = 1.26831(13) \text{ \AA}$  (Rehfuss et al. 1988), which are both significantly longer than neutral  $\text{C}_2$ ,  $r_{\text{CC}} = 1.24244(1) \text{ \AA}$  (Douay et al. 1988). Moreover, the ionicity, defined as the ratio of the molecular dipole moment to the dipole moment resulting from unit point charges separated by the metal- $\text{C}_2$  bond length,  $i = \mu/er_{\text{Mg}-\text{C}_2} = 0.86$ , suggests nearly

<sup>1</sup> We adopt  $N(\text{H}_2) = 2.1 \times 10^{21} \text{ cm}^{-2}$  following Gong et al. (2015).

complete transfer of a  $3s$  electron from Mg to the  $C_2$  fragment.

The bonding in  $MgC_2$  closely resembles that in  $MgO$  (Boldyrev & Simons 1997), with the in-plane  $\pi_u$  orbital of  $C_2$  taking the place of the  $2p_z$  orbital of O.  $MgO$  has a similar ionicity,  $i = 0.72$ , and Mg nuclear quadrupole coupling constant:  $-10(4)$  MHz (Törring & Hoefft 1986) versus  $\chi_{aa} = -11.72(2)$  MHz for  $MgC_2$ . These latter parameters indicate that the Mg  $3s$  orbital in both molecules is substantially hybridized. Given that the atomic  $3p_z$  orbital of  $Mg^+$  has a quadrupole coupling constant of  $-46$  MHz (Sur et al. 2005), the  $p$  character is about 25%. Although simple orbital descriptions of  $MgC_2$  and  $MgO$  are potentially obscured by their multiconfigurational, mixed ionic-covalent character (Thümmel et al. 1989; Itono et al. 2000), this issue appears to be less severe for  $MgC_2$ , which is adequately described with single-reference coupled cluster methods as borne out by the calculations in this work and others (Woon 1996). The bonding of the heavier Group IIA dicarbides  $CaC_2$  and  $SrC_2$  can be expected to follow the same trends observed in their respective oxides. Because of their high ionicities, all of these species possess unusually large dipole moments (Fuentelba & Savin 2000).

Observations of  $MgC_2$  and similar metal dicarbides are a promising means to elucidate the role of metals in the chemistry of IRC+10216, as well as the state of refractory elements in carbon-rich circumstellar environments more generally. Metals are inferred to be significantly depleted onto dust grains in IRC+10216 (Mauron & Huggins 2010), yet even the residual gas-phase abundance of metal atoms and ions is sufficient to drive a rich chemistry. For example, molecules containing the cyano radical (CN) bonded to the most abundant metallic elements (Na, K, Mg, Ca, Al, and Fe) have been found there. Given that the abundances of  $MgC_2$  and  $MgNC$  (Guélin et al. 1995) are within an order of magnitude of each other, it is very likely that other metal dicarbides are also synthesized in the external layers of the circumstellar envelope of IRC+10216, plausibly following the same chemical pathway that is postulated to yield  $MgC_2$ . By analogy with  $SiC_2$ , which has yielded invaluable information on gas-phase processes within the inner and intermediate winds, as well as the outer circumstellar envelopes of evolved carbon-rich stars (Massalkhi et al. 2018, and references therein), metal dicarbides may also serve as important probes provided their excitation, abundance, and distribution are understood. The distribution of metal dicarbides as a function of radial distance from the central star in IRC+10216, for example, accompanied by a careful analysis of their abundance and excitation might shed light on processes

such as condensation and dust formation, which remain poorly understood.

The identification of  $MgC_2$  in the laboratory and in space marks a key step in the study of metal carbides and suggests that other highly polar metal-carbon molecules might be detectable. After  $MgC_2$ ,  $CaC_2$  is the next most promising candidate for detection because it possesses an even larger dipole moment (10.7 D; Fuentelba & Savin (2000)) than  $MgC_2$  (7.9 D; Itono et al. (2000)) and because Ca is cosmically the next most abundant Group IIA element after Mg; calcium isocyanide ( $CaNC$ ) has already been detected in IRC+10216 (Cernicharo et al. 2019), suggesting that other Ca-bearing molecules may be present there. By analogy with  $SiC$  (Massalkhi et al. 2018), the monocarbides  $MgC$  and  $CaC$  may be important for comparative studies of the distribution, abundance, and photochemical processing of dicarbides in circumstellar envelopes; although  $CaC$  has been detected in the laboratory,  $MgC$  has not, and its astronomical detection might be more feasible given the higher abundance of Mg. Other promising systems for study include larger metal-carbon clusters such as  $MgC_n$  about which little is known experimentally, but which, like the silicon-carbon clusters  $SiC_3$  and  $SiC_4$  (Apponi et al. 1999; Gordon et al. 2000), are amenable to laboratory characterization and astronomical detection.



## APPENDIX

## A. STRUCTURE CALCULATIONS AND SEMI-EXPERIMENTAL EQUILIBRIUM GEOMETRY

Coupled cluster calculations were performed using the CFOUR package (Matthews et al. 2020) at the singles, doubles, and perturbative triples (CCSD(T)) level of theory (Raghavachari et al. 1989) with the cc-pCVXZ ( $X = \text{D, T, Q, 5}$ ) basis sets (Woon & Dunning 1995; Prascher et al. 2011) correlating all but the Mg 1s electrons. The complete basis set equilibrium geometry was estimated by an exponential extrapolation of the entire  $X = \text{D-5}$  sequence. To derive a semi-experimental equilibrium geometry, vibrational corrections to the rotational frequencies were determined by variational rovibrational calculations on a potential energy surface (PES) fitted to 448 CCSD(T)/cc-pCVQZ single-point energies using the NITROGEN package (Changala 2021). Additional contributions to the rotational constants from the rotational  $g$ -tensor (Gauss & Puzzarini 2010) were computed with the cc-pCVTZ basis set, and nuclear electric quadrupole coupling constants with the cc-pCV5Z basis set.

The small number of laboratory transitions observed for each isotopologue is insufficient to determine a complete set of experimental rotational constants. Instead, the structure determination was performed by least-squares fitting directly to the transition frequencies. That is, a proposed equilibrium geometry was used to compute equilibrium rotational constants, which were then corrected by the rotational  $g$ -tensor. These in turn were used to generate rigid-rotor transition frequencies, to which the vibrational corrections from the rovibrational variational calculations were added. These latter corrections are defined as the difference between the variational transition energies and the rigid-rotor transition energies based on the equilibrium geometry of the same PES. They therefore include both vibrational zero-point and centrifugal distortion effects. For  $^{25}\text{MgC}_2$ , the degeneracy-weighted mean of the quadrupole-split energies was used as the hyperfine-free value. The optimized structural parameters are shown in Fig. 1 and compared to the extrapolated CCSD(T) geometry in Table 4. These parameters reproduce the 6 laboratory frequencies with a root-mean-square residual of 0.1 MHz. This is significantly larger than the experimental uncertainty (2 kHz) indicating that the theoretical corrections are the dominant source of error.

## B. TWO-TEMPERATURE MODEL FOR ROTATIONAL EXCITATION

In the analysis of rotational emission of prolate asymmetric tops such as  $\text{MgC}_2$  the partitioning of energy levels within and across radiatively decoupled rotational manifolds must be taken into account. Because radiative transitions are confined within the  $K$  ladders but collisional transitions occur within and across the ladders, the rotational excitation temperature within the ladders ( $T_{\text{rot}}$ ) is not necessarily equal to the excitation temperature across the ladders, which is assumed equal to the kinetic temperature ( $T_{\text{kin}}$ ) of the gas. For highly polar species, excitation within the ladders is highly subthermal (i.e.,  $T_{\text{rot}} \ll T_{\text{kin}}$ ) because collisional excitation is much slower than spontaneous radiative decay. Let  $T_{\text{kin}}$  describe the population distribution across  $K$  ladders and  $T_{\text{rot}}$  describe the population distribution within each  $K$  ladder. Then, the intensity of an optically thin rotational line is given by

$$\frac{3kW}{8\pi^3\nu S\mu^2} = \frac{Ne^{-E_J/kT_{\text{rot}}}e^{-E_K/kT_{\text{kin}}}}{Z} \quad (\text{B1})$$

where  $W = \int T_{\text{MB}} dv$  is the main beam temperature integrated over the radial velocity,  $\nu$  is the line frequency,  $S$  is the rotational line strength,  $\mu$  is the dipole moment, and  $N$  is the total column density. The Boltzmann factors and partition function,  $Z$ , in Eq. B1 are calculated by splitting the total rotational energy into two parts,  $E_u = E_K + E_J$ , where  $E_K = (A - (B + C)/2)K^2$  is the  $K$ -dependent part, and  $E_J$  is the remainder. Taking the logarithm of Eq. B1 yields

$$\log \frac{3kW}{8\pi^3\nu S\mu^2} = \log \frac{N}{Z} - \frac{(E_u - E_K) \log e}{kT_{\text{rot}}} - \frac{E_K \log e}{kT_{\text{kin}}}. \quad (\text{B2})$$

A least squares fit of equation B2 to the integrated intensities ( $W$ ) from Table 2 yields  $T_{\text{rot}} = 5.71 \pm 1.12$  K and  $T_{\text{kin}} = 22.14 \pm 13.08$  K, which are shown rounded off in the rotational temperature diagram of Fig. 5. Multiplying the intercept  $\log(N/Z) = 10.60$  by the partition function  $Z(T_{\text{rot}}, T_{\text{kin}}) = 24.59$  evaluated numerically as a sum over states, yields  $N(\text{MgC}_2) = 1 \times 10^{12} \text{ cm}^{-2}$ . We estimate the total uncertainty in  $N$  from the dipole moment ( $7.9 \pm 1.0$  D) and excitation conditions to be 30%.

### C. ACKNOWLEDGMENTS

We thank Dr. Marie-Aline Martin-Drumel (CNRS) for her valuable assistance with the initial laboratory efforts and comments on the manuscript. P.B.C. and M.C.M. are supported by the National Science Foundation (award nos. AST-1908576 and PHY-2110489). H.G. acknowledges support from the National Science Foundation for participation in this work as part of his independent research and development plan. Any opinions, findings, and conclusions expressed in this material are those of the authors and do not necessarily reflect the views of the National Science Foundation. We acknowledge funding support from the Spanish Ministerio de Ciencia e Innovación through grants PID2019-107115GB-C21 and PID2019-106110GB-I00.

## REFERENCES

- Apponi, A. J., McCarthy, M. C., Gottlieb, C., & Thaddeus, P. 1999, *ApJ*, 516, L103
- Bochsler, P., Gonin, M., Sheldon, R. B., et al. 1996, *AIP Conference Proceedings*, 382, 199
- Boldyrev, A. I., & Simons, J. 1997, *J. Phys. Chem. A*, 101, 2215. <https://pubs.acs.org/doi/abs/10.1021/jp962907i>
- Brünken, S., Müller, H. S. P., Menten, K. M., McCarthy, M. C., & Thaddeus, P. 2008, *ApJ*, 676, 1367. <http://www.astro.uni-koeln.de/vorhersagen>.
- Cabezas, C., Cernicharo, J., Alonso, J. L., et al. 2013, 775, 133
- Cernicharo, J., Cabezas, C., Pardo, J., Agúndez, M., & Bermúdez, C. e. a. 2019, *Astron. Astrophys.*, 630, L2
- Cernicharo, J., Guélin, M., & Pardo, J. R. 2004, *Astron. Astrophys.*, 615, L145
- Cernicharo, J., Guélin, M., Kahane, C., et al. 1991, *Astron. Astrophys.*, 246, 213
- Changala, P. B. 2021, *NITROGEN*, version 2.1, <https://github.com/bchangala/nitrogen>
- Crabtree, K. N., Martin-Drumel, M.-A., Brown, G. G., et al. 2016, *J. Chem. Phys.*, 144, 124201. <http://scitation.aip.org/content/aip/journal/jcp/144/12/10.1063/1.4944072>
- Douay, M., Nietmann, R., & Bernath, P. F. 1988, *J. Mol. Spectrosc.*, 131, 250
- Dunbar, R. C., & Petrie, S. 2002, *Astrophys. J.*, 564, 792
- Fuentealba, P., & Savin, A. 2000, *J. Phys. Chem. A*, 104, 10882
- Gauss, J., & Puzzarini, C. 2010, *Mol. Phys.*, 108, 269
- Gong, Y., Henkel, C., & Spezzano, S. e. a. 2015, *Astron. Astrophys.*, 574, A56
- Gordon, V. D., Nathan, E. S., Apponi, A. J., et al. 2000, *J. Chem. Phys.*, 113, 5311
- Grabow, J. U., Palmer, E. S., McCarthy, M. C., & Thaddeus, P. 2005, *Rev. Sci. Instrum.*, 76, 093106
- Green, M. L., Jaffe, N. B., & Heaven, M. C. 2020, *J. Phys. Chem. Lett.*, 11, 88
- Green, S. 1984, *Chem. Phys. Lett.*, 112, 29
- Guélin, M., Forestini, M., Valiron, P., et al. 1995, *Astron. Astrophys.*, 297, 183
- Guélin, M., Patel, N. A., Bremer, M., et al. 2018, *A&A*, 610, A4
- Halfen, D. T., Min, J., & Ziurys, L. M. 2013, *Chem. Phys. Lett.*, 555, 31
- Halfen, D. T., & Ziurys, L. M. 2018, *Phys. Chem. Chem. Phys.*, 20, 11047
- Itono, S., Takano, K., Hirano, T., & Nagashima, U. 2000, *ApJL*, 538, L163. <https://ui.adsabs.harvard.edu/abs/2000ApJ...538L163I/abstract>
- Kawaguchi, K., Kagi, E., Hirano, T., Takano, S., & S., S. 1993, *ApJ*, 406, L39
- Kleman, B. 1956, *ApJ*, 123, 162
- Lee, K. L. K., Thorwirth, S., Martin-Drumel, M. A., & McCarthy, M. C. 2019, *Phys. Chem. Chem. Phys.*, 21, 18911. <https://pubs.rsc.org/en/content/articlehtml/2019/cp/c9cp03607e><https://pubs.rsc.org/en/content/articlelanding/2019/cp/c9cp03607e>
- Massalkhi, S., Agúndez, M., & Cernicharo, J. e. a. 2018, *Astron. Astrophys.*, 630, A29
- Matthews, D. A., Cheng, L., Harding, M. E., et al. 2020, *J. Chem. Phys.*, 152, 214108
- Mauron, N., & Huggins, P. J. 2010, *Astron. Astrophys.*, 513, A31. <https://www.aanda.org/articles/aa/abs/2010/05/aa13970-09/aa13970-09.html>
- Millar, T. J. 2008, *Astrophys. Space Sci.*, 313, 223. <https://link.springer.com/article/10.1007/s10509-007-9636-z>
- Min, J., Halfen, D. T., & Ziurys, L. M. 2014, *Chem. Phys. Lett.*, 609, 70. <https://ui.adsabs.harvard.edu/abs/2014CPL...609...70M/abstract>
- Pardo, J. R., Cabezas, C., Fonfría, J. P., et al. 2021, *Astron. Astrophys.*, 652, L13
- Pardo, J. R., Cernicharo, J., Tercero, B., et al. 2022, *Astron. Astrophys.*, 658, A39
- Patel, N. A., Young, K. H., Gottlieb, C. A., et al. 2011, *Astrophys. J. Suppl. Ser.*, 193, 17. <https://iopscience.iop.org/article/10.1088/0067-0049/193/1/17><https://iopscience.iop.org/article/10.1088/0067-0049/193/1/17/meta>
- Petrie, S. 1996, *Mon. Not. R. Astron. Soc.*, 282, 807. <https://ui.adsabs.harvard.edu/abs/1996MNRAS.282..807P/abstract>
- Prascher, B. P., Woon, D. E., Peterson, K. A., Dunning, T. H., & Wilson, A. K. 2011, *Theor. Chem. Acc.*, 128, 69. <https://link.springer.com/article/10.1007/s00214-010-0764-0>
- Raghavachari, K., Trucks, G. W., Pople, J. A., & Head-Gordon, M. 1989, *Chem. Phys. Lett.*, 157, 479. <https://www.sciencedirect.com/science/article/pii/S0009261489873956?via%3Dihub>
- Rehfuß, B. D., Liu, D. J., Dinelli, B. M., et al. 1988, *J. Chem. Phys.*, 89, 129
- Sun, M., Halfen, D. T., Min, J., et al. 2010, *J. Chem. Phys.*, 133, 174301
- Sur, C., Sahoo, B. K., Chaudhuri, R. K., Das, B. P., & Mukherjee, D. 2005, *Eur. Phys. J. D*, 32, 25. <https://link.springer.com/article/10.1140/epjd/e2004-00176-1>
- Thaddeus, P., Cummins, S. E., & Linke, R. A. 1984, *ApJ*, 23, L45

Thümmel, H., Klotz, R., & Peyerimhoff, S. D. 1989, Chem. Phys., 129, 417  
Törring, T., & Hoefft, J. 1986, Chem. Phys. Lett., 126, 477  
Woon, D. E. 1996, Astrophys. J., 456, 602  
Woon, D. E., & Dunning, T. H. 1995, J. Chem. Phys, 103, 4572

Zingsheim, O., Martin-Drumel, M. A., Thorwirth, S., et al. 2017, J. Phys. Chem. Lett., 8, 3776

Ziurys, L. M., Apponi, A. J., Guélin, M., & Cernicharo, J. 1995, ApJ, 445, L47



**Table 1.** Laboratory rotational frequencies of  $\text{MgC}_2$ .

Isotopologue	Transition		Frequency (MHz)
	$J'_{K_a K_c} - J''_{K_a K_c}$	$F' - F''$	
$^{24}\text{Mg}^{12}\text{C}_2$	$1_{01} - 0_{00}$	$\dots$	20896.090(2)
	$2_{02} - 1_{01}$	$\dots$	41711.852(4)
$^{24}\text{Mg}^{13}\text{C}^{12}\text{C}$	$1_{01} - 0_{00}$	$\dots$	20443.702(2)
$^{24}\text{Mg}^{13}\text{C}_2$	$1_{01} - 0_{00}$	$\dots$	20027.207(2)
$^{25}\text{Mg}^{12}\text{C}_2$	$1_{01} - 0_{00}$	$2.5 - 2.5$	20509.780(4)
		$3.5 - 2.5$	20512.245(4)
		$1.5 - 2.5$	20513.305(4)
$^{26}\text{Mg}^{12}\text{C}_2$	$1_{01} - 0_{00}$	$\dots$	20157.202(2)

NOTE—Estimated uncertainties are given in parentheses in units of the last digit.

**Table 2.** Lines of MgC<sub>2</sub> in IRC+10216

Isotopologue	Transition	$\nu_{\text{obs}}^a$	$\nu_{\text{obs-calc}}$	$E_u/k$	$S$	$\int T_{\text{A}}^* dv^b$	$\theta_{\text{B}}$	$\eta_{\text{B}}$	$W^c$
	$J'_{K_a K_c} - J''_{K_a K_c}$	(MHz)	(MHz)	(K)		(mK km s <sup>-1</sup> )	( $''$ )		(mK km s <sup>-1</sup> )
<sup>24</sup> MgC <sub>2</sub>	2 <sub>02</sub> – 1 <sub>01</sub>	41711.82 ± 0.02	−0.034	3.00	2.00	221 ± 10	42.5	0.53	1254 ± 138
	4 <sub>04</sub> – 3 <sub>03</sub>	82787.94 ± 0.02	0.015	9.97	3.99	362 ± 10	29.7	0.853	841 ± 87
	4 <sub>23</sub> – 3 <sub>22</sub>	83511.00 ± 0.15	−0.096	17.98	3.00	108 ± 11	29.5	0.853	249 ± 36
	4 <sub>22</sub> – 3 <sub>21</sub>	84304.13 ± 0.04	0.105	18.04	3.00	149 ± 9	29.2	0.853	340 ± 40
	5 <sub>05</sub> – 4 <sub>04</sub>	102907.74 ± 0.10	0.137	14.91	4.98	248 ± 8	23.9	0.853	476 ± 50
	5 <sub>42</sub> – 4 <sub>41</sub> <sup>d</sup>	104610.76 ± 0.30	−0.463	46.88	1.80	35 ± 8	23.5	0.853	65 ± 16
	5 <sub>41</sub> – 4 <sub>40</sub> <sup>d</sup>	104610.76 ± 0.30	−0.762	46.88	1.80	35 ± 8	23.5	0.853	65 ± 16
	5 <sub>23</sub> – 4 <sub>22</sub>	105852.05 ± 0.15	−0.338	23.12	4.20	164 ± 9	23.2	0.853	308 ± 35
	6 <sub>06</sub> – 5 <sub>05</sub>	122684.00 ± 0.50	−0.084	20.80	5.97	251 ± 30	20.1	0.785	463 ± 89
	7 <sub>07</sub> – 6 <sub>06</sub>	142108.88 ± 0.10	−0.077	27.62	6.96	83 ± 6	17.3	0.785	141 ± 23
	7 <sub>25</sub> – 6 <sub>24</sub>	149761.18 ± 0.20	−0.189	36.43	6.43	38 ± 7	16.4	0.785	63 ± 15
<sup>25</sup> MgC <sub>2</sub>	2 <sub>02</sub> – 1 <sub>01</sub>	40949.33 ± 0.20	−0.267	3.00	2.00	34 ± 5	42.5	0.53	193 ± 34
<sup>26</sup> MgC <sub>2</sub>	2 <sub>02</sub> – 1 <sub>01</sub>	40245.20 ± 0.20	−0.085	2.90	2.00	46 ± 8	42.5	0.53	261 ± 52
	4 <sub>04</sub> – 3 <sub>03</sub>	79942.90 ± 0.30	0.171	9.62	3.99	41 ± 13	29.7	0.853	99 ± 33
	5 <sub>05</sub> – 4 <sub>04</sub>	99428.70 ± 0.40	−0.138	14.40	4.98	45 ± 10	29.7	0.853	89 ± 22

NOTE—Unless otherwise noted, estimated uncertainties are  $1\sigma$ . Frequencies subtracted from those observed are calculated from the constants in Table 3.  $E_u$  is the energy of the upper state of the transition, and  $S$  is the asymmetric rotor line strength.  $\alpha_{\text{J2000}} = 09^{\text{h}}47^{\text{m}}57^{\text{s}}.36$ ,  $\delta_{\text{J2000}} = +13^{\circ}16'44.''4$ .

<sup>a</sup>On the assumption of  $v_{\text{LSR}} = -26.5 \text{ km s}^{-1}$ .

<sup>b</sup>Derived from least-squares fits of shell profiles to the spectra shown in Figs. 3 and 4; in some cases the expansion velocity was fixed to  $14.5 \text{ km s}^{-1}$ .

<sup>c</sup> $W = \int T_{\text{A}}^* dv / \eta_{\text{B}} f_{\text{D}}$ , where  $f_{\text{D}} = \theta_{\text{S}}^2 / (\theta_{\text{S}}^2 + \theta_{\text{B}}^2)$  and the source diameter  $\theta_{\text{S}} = 30''$ . Errors include calibration uncertainties of 10% at 7 mm, 10% at 3 mm, and 15% at 2 mm, as well as an assumed error of 1 D on the dipole moment, added in quadrature.

<sup>d</sup>Unresolved doublet with each component assumed to lie at the same frequency and possess half the intensity.

**Table 3.** Spectroscopic Constants of  $\text{MgC}_2$ 

Constant	$^{24}\text{MgC}_2$	$^{25}\text{MgC}_2$	$^{26}\text{MgC}_2$
Rotational and centrifugal distortion constants (MHz):			
$A$ . . . . .	51900(1)	51899.8 <sup>b</sup>	51897.6 <sup>b</sup>
$(B + C)/2$	10448.0740(9)	10255.8294(12)	10078.601(1)
$(B - C)/4$	526.033(14)	507.046 <sup>b</sup>	490.890(61)
$10^3\Delta_J$ . . .	14.454(101)	...	...
$10^3\Delta_{JK}$ . .	245.12(169)	...	...
$10^3\Delta_K$ . . .	-37.84 <sup>a</sup>	...	...
$10^3\delta_J$ . . . .	0.369(168)	...	...
$10^3\delta_K$ . . . .	148.03 <sup>a</sup>	...	...
Electric quadrupole coupling constants (MHz):			
$\chi_{aa}$ . . . . .	...	-11.75(2)	...
$\chi_{bb}$ . . . . .	...	4.8(10)	...
$\sigma_{\text{nrms}}$ . . . . .	1.37	0.29	0.40
Inertial defect ( $\text{amu}\cdot\text{\AA}^2$ ):			
$\Delta$ . . . . .	0.1035(3)	0.1037	0.125(1)

NOTE—Constants are derived from a least-squares fit to the rotational transitions in Tables 1 and 2. The  $1\sigma$  uncertainties are indicated in parentheses, with the least significant digit corresponding to the least significant digit of the value. Parameters for which no errors are indicated have been fixed to the theoretical values.

<sup>a</sup>Second-order vibrational perturbation theory (VPT2) value at the CCSD(T)/cc-pVTZ level of theory.

<sup>b</sup>Fixed to the experimental values derived from  $^{24}\text{MgC}_2$ : the equilibrium isotope shift was taken from the semi-experimental equilibrium structure, and the zero-point correction from the variational calculations (Appendix A).

**Table 4.** The equilibrium geometry of  $\text{MgC}_2$ .

Basis set	$r_{\text{CC}}$	$r_{\text{Mg-C}_2}$
D	1.29422	1.96504
T	1.27545	1.92117
Q	1.27175	1.91073
5	1.27082	1.90741
CBS	1.27068	1.90673
$r_{\text{se}}$	1.2706(7)	1.9066(1)

NOTE—The CCSD(T)/cc-pCVXZ bond lengths (in  $\text{\AA}$ ) are shown for  $X = \text{D-5}$ , followed by the complete basis set (CBS) extrapolation. The semi-experimental equilibrium geometry ( $r_{\text{se}}$ ) was determined as discussed in the text.  $r_{\text{CC}}$  is the C-C distance and  $r_{\text{Mg-C}_2}$  is the distance between Mg and the CC center-of-mass.

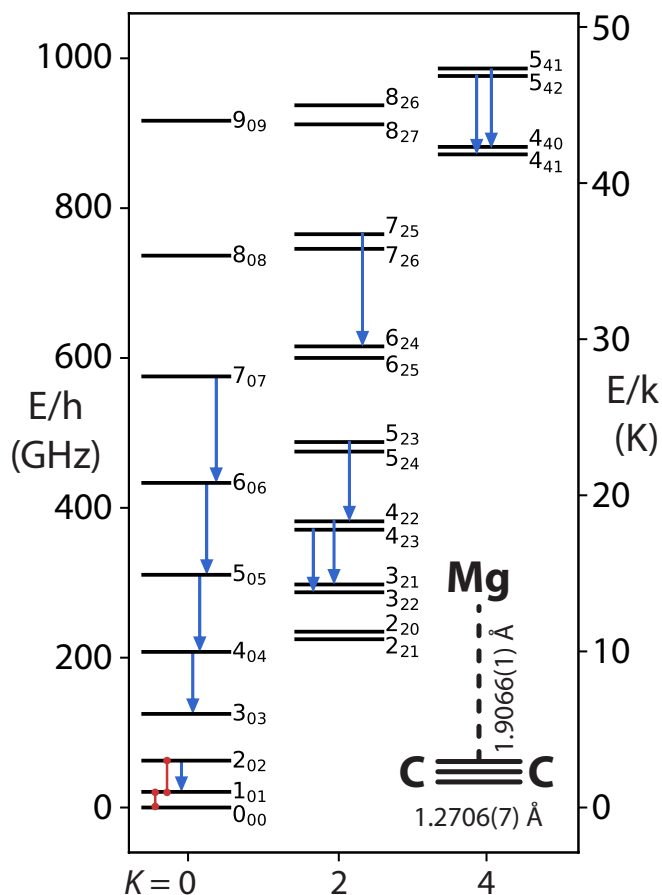


**Figure 1.** Lower rotational energy levels of  $\text{MgC}_2$ . Red lines indicate the observed laboratory transitions and blue arrows the astronomical transitions. The inset shows the semi-experimental equilibrium structure.

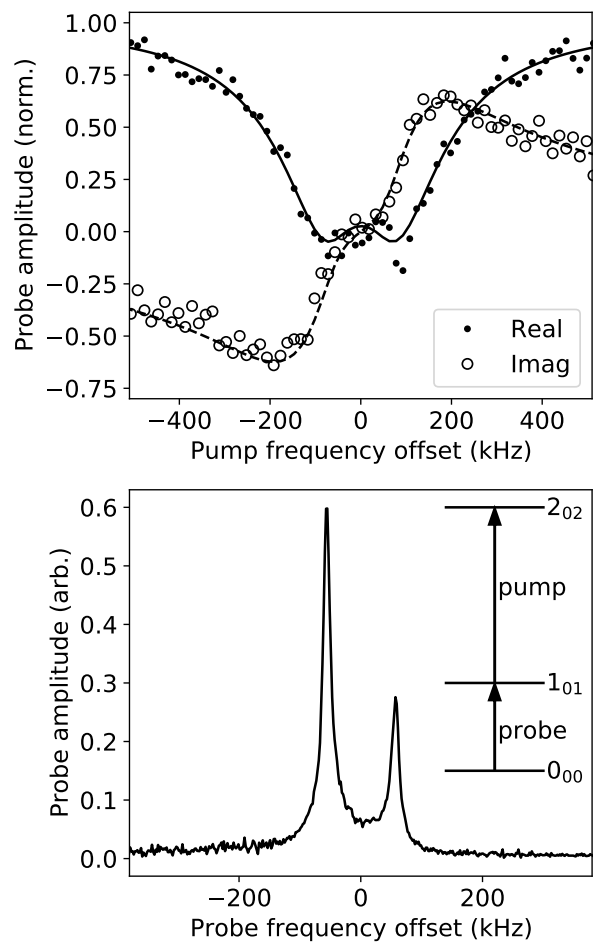


**Figure 2.** Laboratory measurements of the two lowest rotational transitions of  $^{24}\text{MgC}_2$ . The cavity-FTMW signal (bottom) centered at 20896.090 MHz is split into two Doppler components due to the co-axial cavity geometry. Its complex amplitude response (top) is plotted as a function of the double resonance pump frequency relative to 41711.852 MHz. The solid and dashed curves are the fitted saturated Lorentzian line profiles for the real and imaginary parts, respectively. Each panel represents 6.5 h of integration or about 120,000 laser shots.

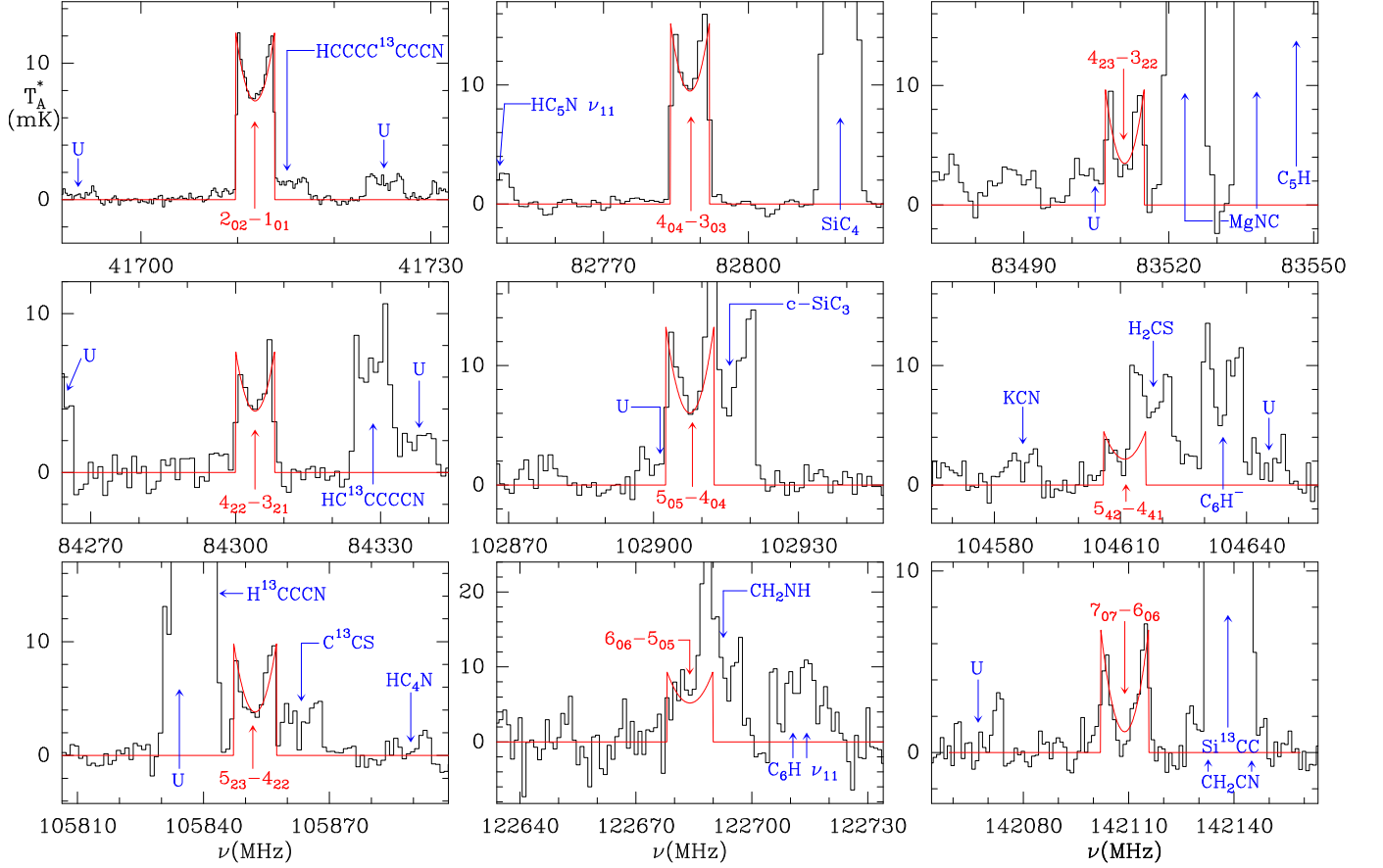


**Figure 3.** Spectra of  $^{24}\text{MgC}_2$  toward IRC+10216. The fitted profiles are plotted in red. ‘U’ indicates unidentified lines.

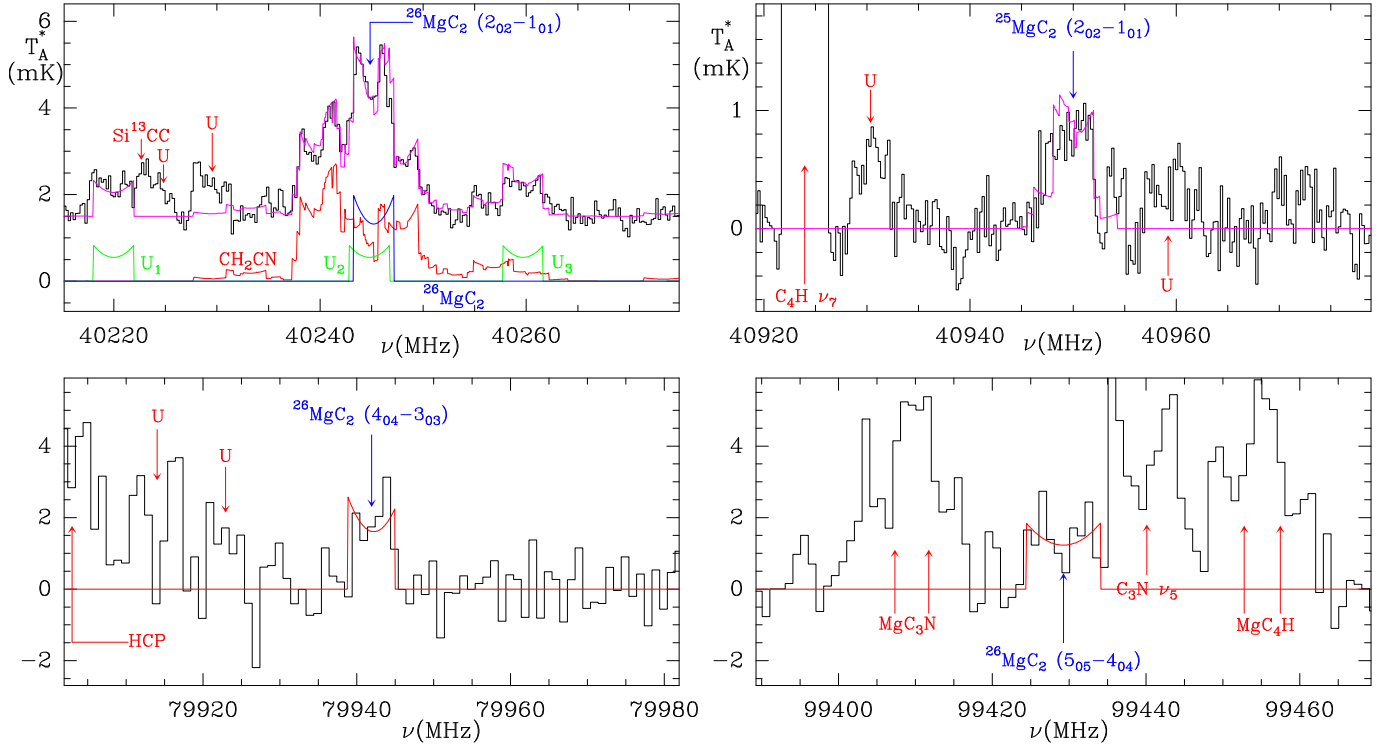


**Figure 4.** Spectra of  $^{25}\text{MgC}_2$  and  $^{26}\text{MgC}_2$  toward IRC+10216. The simulated profile of the  $2_{02} - 1_{01}$  transition of  $^{26}\text{MgC}_2$  (shown in blue in the top left panel) accounts for contamination from overlapping  $\text{CH}_2\text{CN}$  transitions (shown in red); the total emission is shown in magenta. The profile for  $^{25}\text{MgC}_2$  (top right) includes quadrupole hyperfine splittings calculated from the laboratory constants. ‘U’ indicates unidentified lines.



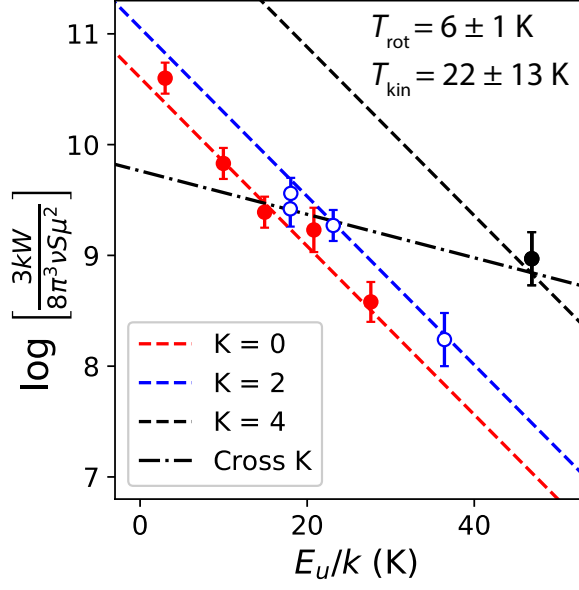


**Figure 5.** Rotational temperature diagram of  $^{24}\text{MgC}_2$  in IRC+10216, fitted with the two-temperature model described in Appendix B. The slope of the parallel lines through each  $K$  ladder yields the rotational temperature ( $T_{\text{rot}}$ ), and the slope of the line through points across the  $K$  ladders yields the kinetic temperature ( $T_{\text{kin}}$ ). The flux of the  $K = 4$  transition is assumed to be one-half the total flux of the unresolved  $5_{42} - 4_{41}/5_{41} - 4_{40}$  doublet. The error bar on each data point is twice the error shown in Table 2. Error bars on the parameters are twice the standard error of the fit.